# Photoinduced processes in dye-sensitized photoanodes under the spotlight: a multiscale in silico investigation

Menzel, J.P.

# CHAPTER 7

# Conclusions and Outlook

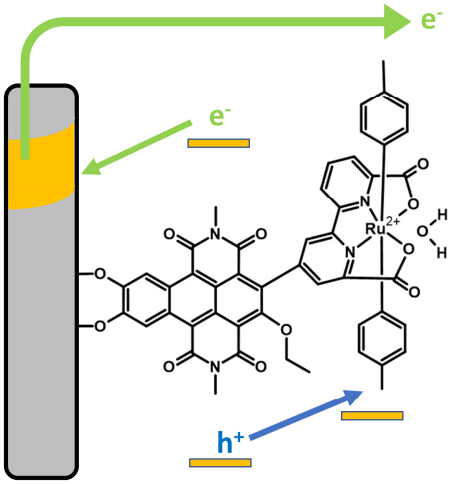


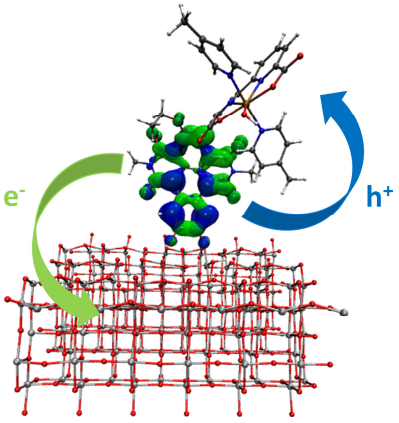


***This Chapter is based in part on:***

Jan Paul Menzel, Justina Moss, Jelena Belić, Huub J.M. de Groot, Lucas Visscher, Francesco Buda; *in preparation*

# 7

## 7.1 Conclusions

Increasing the efficiency of Dye-Sensitized Photoelectrochemical Cells remains a prime objective in solar fuel production.[1] Using computational methods to design and optimize the different components and interfaces in a dye-sensitized photoanode can support and facilitate experimental work in assembling and improving these devices.[2–4] This work aims at moving further towards this goal and several steps have been executed

In **chapter 3**, the fundamental process of photoinduced coherent charge transfer was investigated in a pseudo base pair donor-acceptor molecular complex to understand the requirements for this ultrafast process. Our simulations underline how nuclear modes vibronically couple to the electronic system and drive population exchange from the exciton to the charge transfer state.[5] Through adjusting the frequency of the relevant nuclear vibrations by isotope exchange, we successfully modulated the resonance associated to the coherent charge transfer process and disentangled how nuclear modes are selected. The importance of symmetry is revealed, as we find that coherent charge transfer requires dynamical symmetry breaking to proceed. This suggests that chiral systems should be preferred when trying to take advantage of ultrafast coherent charge transfer. We also find evidence of angular momentum exchange between the (classical) nuclear and (quantum mechanical) electronic subsystems.[6]

Photoinduced electron injection into a $TiO_2$ semiconductor sensitized by several NDI-based dyes were simulated in **chapter 4**. For these simulations, a computational strategy was developed using a combination of DFTB[7–10] based nuclear dynamics and quantum propagation using the AO/MO propagator and an extended Hückel Hamiltonian.[11–13] We find that nuclear dynamics and trajectory averaging are crucial for a realistic description of the injection process. Furthermore, explicit solvation is important for the correct exploration of conformational space in the nuclear dynamics. Taking these findings into account, the semi-empirical quantum-classical simulation of photoinduced electron injection can be used for qualitative

determination of electron injection capabilities of anchoring groups and potential molecular chromophores.[14]

In **chapter 5**, an efficient approach to calculate Gibbs free energy differences and oxidation potentials in a ruthenium-based water oxidation catalyst has been introduced. In this workflow, GFN-xTB[15] is used for geometry optimizations and frequency analysis, followed by a single point calculation by a higher-level method, such as B3LYP based DFT,[16,17] to determine Gibbs free energies of all catalytic intermediates. The method predicts the experimentally determined catalytic cycle and reaction mechanism and gives Gibbs free energy differences in close agreement with full B3LYP/DFT results, while reducing the computational cost by 2 orders of magnitude. Oxidation potentials determined by this approach also agree very well with experimental results.[18]

To decrease charge recombination losses, push-pull dyes can be used to spatially separate electron and hole.[19–22] A family of such dyes consisting of polyphenylamine donors, fluorene bridges and perylene monoamide acceptors was investigated in **chapter 6**. We performed a systematic investigation on the effects of different molecular designs on the charge separation efficiency. We found that increasing the electron donating character of substituents on the donor increase the charge separation efficiency considerably. While using a TPA vs. DPA anchor does not increase the hole transfer from the acceptor, more hole density localizes at the donor rather than the bridge, leading to a larger polarization of the molecule. Increasing the bridge length by a second additional fluorene moiety leads to a better charge separation in comparison to the molecule with one fluorene, with more hole density residing on the fluorene and donor and less back transfer to the PMI, while a further increase in the number of fluorenes towards 3 does not increase further the performance. Decoupling the different components by breaking conjugation through methyl groups forcing the dihedral angles between the components close to 90 degrees also leads to a better charge separation in comparison to the planar molecule, especially when the fluorene is equipped with methyl groups. An *in silico*

optimization of a nonplanar charge separating dye was then performed, taking advantage of the insight gained by the systematic investigations, resulting in a significant increase of charge separation capability compared to planar systems.

Simulating at an atomistic level the whole photocatalytic water splitting reaction at the photoanode of a DS-PEC device remains a challenging task due to the large size of the system, and the broad range of time scales of the complex processes involved that require different computational approaches. In this work we have made significant progress in simulating a dye sensitized photoanode, including semiconductor, anchor molecule, molecular dye and taking into account the electrolyte environment. With the semiclassical multiscale approach that combines tight binding based nuclear dynamics with quantum propagation of electron and hole, simulations of charge migration in a full photoanode system become viable, while remaining flexible and reliable due to its parametrization on either experimental redox potentials or higher level computational methods.

## 7.2 Outlook

*Charge Transfer in a Photocatalytic Dye-WOC Complex*

While we investigated the photoinduced electron injection from an NDI-based dye into a semiconductor electrode in chapter 4 and showed that GFN-xTB is a viable method for geometries and frequencies of a ruthenium based WOC, it would be interesting to combine these two approaches to investigate the hole transfer in a photocatalytic dye-WOC complex upon irradiation. An example of such a photocatalytic molecular complex is given in scheme 7.1.

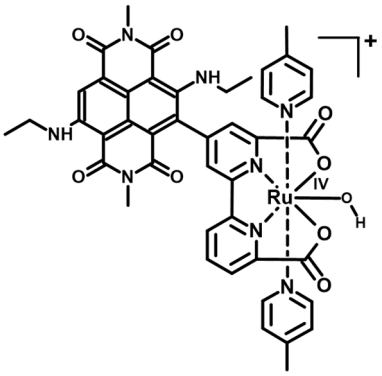


**Scheme 7.1.** Example of a molecular photocatalytic water splitting complex consisting of the WOC investigated in chapter 5 and an NDI based dye, here with two ethylamino groups, connected via a core carbon to the WOC.

Simulating this hole transfer is quite challenging due to several properties intrinsic to the WOC's catalytic cycle and the chemical environment. First, the HOMO and LUMO energies of the WOC change quite significantly over the course of the catalytic steps, as the WOC oxidizes the water and is itself oxidized by the photoexcited dye. This is sketched in scheme 7.2.

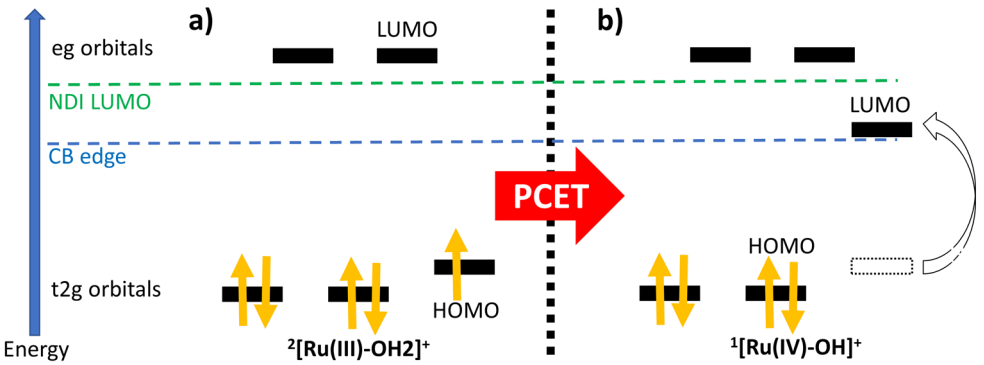


**Scheme 7.2.** Electron configuration and HOMO/ LUMO energies of the ruthenium based WOC for different catalytic intermediates. The singly occupied HOMO of the $^{2}$[Ru(III)-$OH_2$]$^{+}$ (**a**) has a higher energy and the complex is thus more easily oxidized by a photoexcited dye compared to the catalytic intermediate $^{1}$[Ru(IV)-OH]$^{+}$ (**b**). After the PCET step indeed the third t2g orbital is slightly higher energetically due to the deformed octahedral environment. Additionally, the unoccupied orbital is pushed up in energy as the geometric structure relaxes towards a new minimum with the new electron configuration. The LUMO energy of the $^{1}$[Ru(IV)-OH]$^{+}$ is therefore significantly lower than the LUMO of the $^{2}$[Ru(III)-$OH_2$]$^{+}$, closely above the conduction band edge of $TiO_2$.

The challenge is that the same molecular dye needs to have enough oxidative power to drive the WOC through its entire cycle. Since here, we use a WOC that reacts via a radical coupling mechanism, only two oxidative states are relevant for photooxidation. However, their respective HOMO and LUMO energies change significantly. The HOMO of the $^{2}$[Ru(III)-$OH_2$]$^{+}$, is unoccupied in the $^{1}$[Ru(IV)-OH]$^{+}$, and is pushed up in energy through geometric rearrangement of the WOC, such that the resulting LUMO of the $^{1}$[Ru(IV)-OH]$^{+}$ is close in energy to the $TiO_2$ conduction band edge, below the LUMO energies of feasible molecular dyes (see Scheme 7.2). This makes the energetic difference between the two oxidative steps quite large and finding suitable dyes a challenging task. Another problem is the influence of the pH on the oxidation potential. We have simulated hole transfer from the photoexcited dye to the WOC in the $^{1}$[Ru(IV)-OH]$^{+}$ state, since this is the most difficult to oxidize, with the same method as in chapters 4 and 6, using GFN-xTB as a suitable ground state MD method (see chapter 5). Furthermore, since the

$^{1}$[Ru(IV)-OH]$^{+}$ is in the singlet state, the simulations can be performed in a restricted manner. The Computational details can be found in the appendix. Figure 7.1 shows the photoinduced hole transfer upon exciting the NDI in the dye-WOC complex of scheme 7.1. As is visible, we are able to follow the hole transfer towards the WOC, suggesting that the dye has enough oxidative power when photoexcited to oxidize the $^{1}$[Ru(IV)-OH]$^{+}$. Including full explicit solvation is an obvious next step, which is in progress.

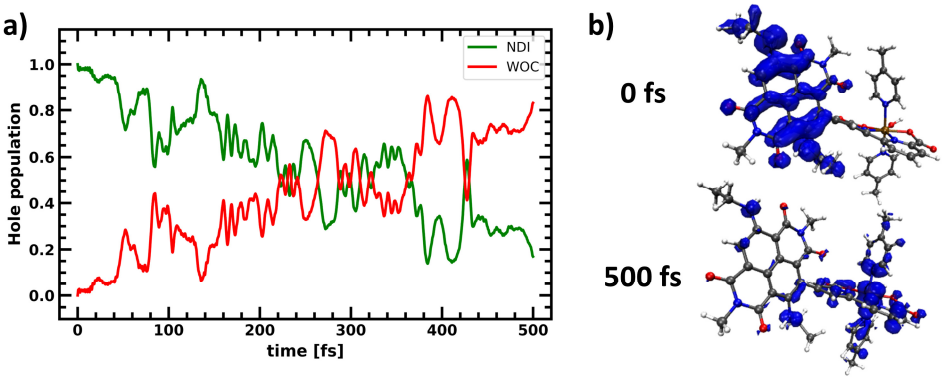


**Figure 7.1. a)** Hole population on the NDI (green) and WOC (red) over time after photoexcitation of the NDI. **b)** initial and final hole density on the complex.

Since the LUMO of the $^{1}$[Ru(IV)-OH]$^{+}$ is energetically close to the LUMO of the NDI, an important challenge is to prevent back transfer of a photoexcited electron from the dye to the WOC, which would enable regeneration of the $^{2}$[Ru(III)-OH$_2$]$^{+}$. We can follow the transfer of a photoexcited electron from the NDI to the WOC in its $^{1}$[Ru(IV)-OH]$^{+}$ state in our simulations, where electron population is transferred from the photoexcited dye towards the WOC, as shown in (figure 7.2).

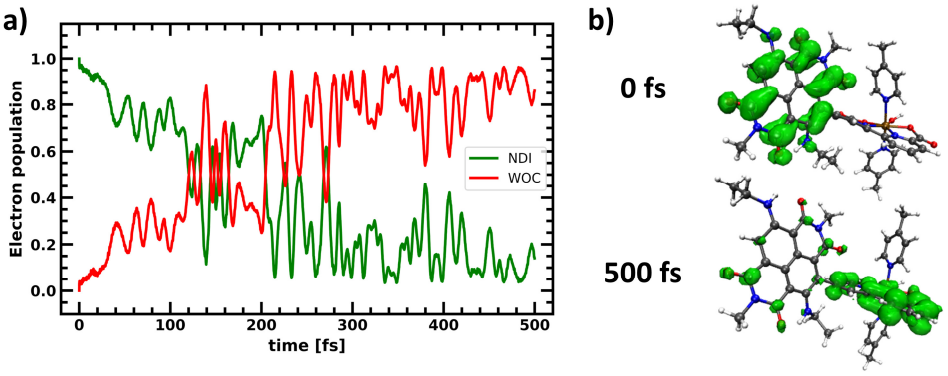


**Figure 7.2. a)** Electron population on the NDI (green) and WOC (red) over time after photoexcitation of the NDI. **b)** initial and final electron density on the complex.

To prevent such a transfer on short time scales, molecular moieties might be included, as discussed in chapter 6, that allow for hole transfer but inhibit electron transfer, such as a molecular barrier, a charge separating bridge, or a molecular rectifier. The search for a suitable module is one of our currently ongoing investigations. It is however quite promising that photoinduced electron and hole transfer in such challenging systems, including a transition metal complex, can be simulated using this quantum-classical, semi-empirical approach.

*Simulating Charge Separation in a Full Photoanode System*

The ultimate goal however would be to follow electron and hole transfer in a full photoanode system, including semiconductor electrode, anchoring group, molecular dye, the WOC, potential charge separating dyes or molecular rectifiers and explicit solvent. The combination of GFN-xTB for the nuclear dynamics and the AO/MO quantum propagation of electron and hole potentially allows for the treatment of such extended systems. We have already been successful in performing simulations of photoinduced electron injection and hole transfer for the system shown in figure 7.3: a semiconductor-dye-WOC complex. Here, we chose the cat-NDI dye from chapter 4, since the LUMO lies energetically well within the conduction band of the $TiO_2$ at a large density of states (figure 4A.3 in the appendix of chapter 4) and the HOMO is

low enough in energy for potential hole transfer to the most demanding catalytic step of the WOC, the $^{1}$[Ru(IV)-OH]$^{+}$ (see chapters 4 and 5).

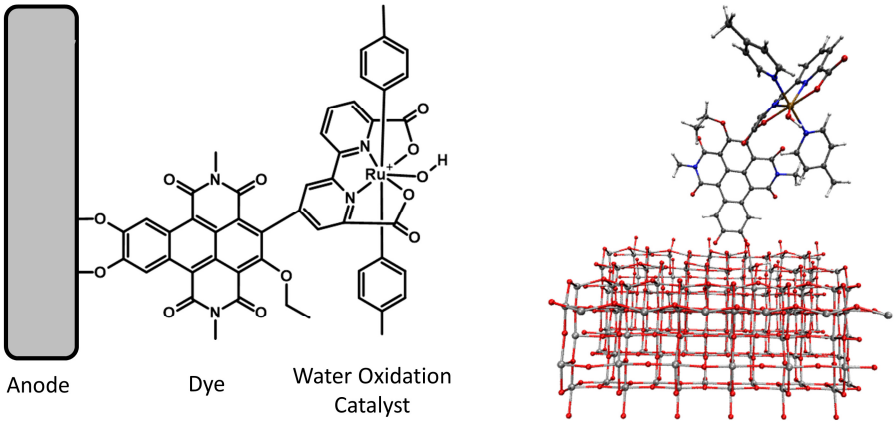


**Figure 7.3.** Chemical structure and geometry of the $TiO_2$-Dye-WOC complex investigated.

Moreover, we expect that for this case the effect of including explicit solvation is relatively minor (see chapter 4). However, for a more rigorous description especially of the interaction between WOC and electrolyte, we are currently working on including explicit solvent. The optimized extended Hückel parameters of chapter 4 were used for the cat-NDI dye, with the optimized parameters for the $^{1}$[Ru(IV)-OH]$^{+}$ from the previous section.

In figure 7.4, electron and hole populations on the different fragments over time are shown after photoexcitation of the dye. As can be seen, electron injection is quite fast and finished within the first 20 fs. The low lying LUMO of the WOC does not seem to be too problematic, as only a low quantity of electron density is donated to the WOC.

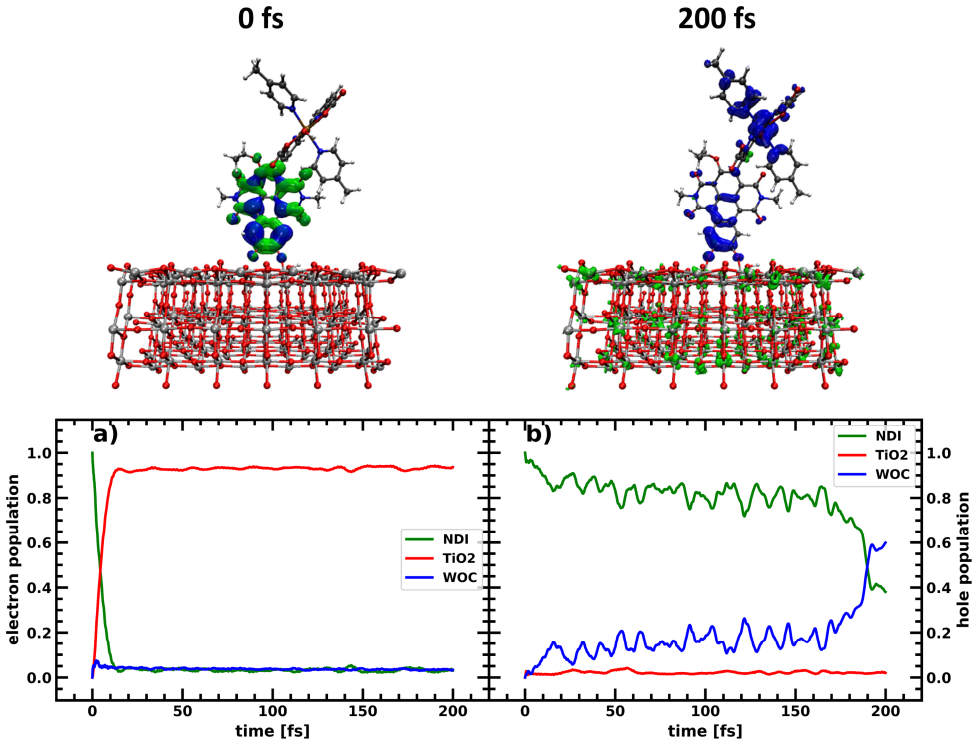


**Figure 7.4. a)** Electron population on the NDI (green), $TiO_2$ (red) and WOC (blue) over time after photoexcitation of the NDI. **b)** Hole population on the NDI (green), $TiO_2$ (red) and WOC (blue) over time after photoexcitation of the NDI. On top the electron (green) and hole (blue) densities at the initial time step and after 200 fs.

Hole transfer takes longer, but after 200 fs, about 50 % of the hole is transferred towards the WOC. While these are only preliminary results, this illustrates the great potential of the semi-empirical, quantum classical approach in simulating photoinduced processes in dye-sensitized photoelectrochemical cells, with an *in silico* treatment of the full photoanode system well within reach.

## 7.3 References


(1) Yu, Z.; Li, F.; Sun, L. Recent Advances in Dye-Sensitized Photoelectrochemical Cells for Solar Hydrogen Production Based on Molecular Components. *Energy Environ. Sci.* **2015**, *8* (3), 760–775. https://doi.org/10.1039/C4EE03565H.

(2) Pastore, M.; Mosconi, E.; De Angelis, F.; Grätzel, M. A Computational Investigation of Organic Dyes for Dye-Sensitized Solar Cells: Benchmark, Strategies, and Open Issues. *J. Phys. Chem. C* **2010**, *114* (15), 7205–7212. https://doi.org/10.1021/jp100713r.

(3) Ding, W.; Koepf, M.; Koenigsmann, C.; Batra, A.; Venkataraman, L.; Negre, C. F. A.; Brudvig, G. W.; Crabtree, R. H.; Schmuttenmaer, C. A.; Batista, V. S. Computational Design of Intrinsic Molecular Rectifiers Based on Asymmetric Functionalization of N-Phenylbenzamide. *J. Chem. Theory Comput.* **2015**, *11* (12), 5888–5896. https://doi.org/10.1021/acs.jctc.5b00823.

(4) Belić, J.; van Beek, B.; Menzel, J. P.; Buda, F.; Visscher, L. Systematic Computational Design and Optimization of Light Absorbing Dyes. *J. Phys. Chem. A* **2020**, *124* (31), 6380–6388. https://doi.org/10.1021/acs.jpca.0c04506.

(5) Rafiq, S.; Scholes, G. D. From Fundamental Theories to Quantum Coherences in Electron Transfer. *J. Am. Chem. Soc.* **2019**, *141* (2), 708–722. https://doi.org/10.1021/jacs.8b09059.

(6) Menzel, J. P.; de Groot, H. J. M.; Buda, F. Photoinduced Electron Transfer in Donor–Acceptor Complexes: Isotope Effect and Dynamic Symmetry Breaking. *J. Phys. Chem. Lett.* **2019**, *10* (21), 6504–6511. https://doi.org/10.1021/acs.jpclett.9b02408.

(7) Porezag, D.; Frauenheim, Th.; Köhler, Th.; Seifert, G.; Kaschner, R. Construction of Tight-Binding-like Potentials on the Basis of Density-Functional Theory: Application to Carbon. *Phys. Rev. B* **1995**, *51* (19), 12947–12957. https://doi.org/10.1103/PhysRevB.51.12947.

(8) Elstner, M.; Porezag, D.; Jungnickel, G.; Elsner, J.; Haugk, M.; Frauenheim, Th.; Suhai, S.; Seifert, G. Self-Consistent-Charge Density-Functional Tight-Binding Method for Simulations of Complex Materials Properties. *Phys. Rev. B* **1998**, *58* (11), 7260–7268. https://doi.org/10.1103/PhysRevB.58.7260.

(9) Elstner, M.; Frauenheim, T.; Kaxiras, E.; Seifert, G.; Suhai, S. A Self-Consistent Charge Density-Functional Based Tight-Binding Scheme for Large Biomolecules. *Phys. Status Solidi B* **2000**, *217* (1), 357–376. https://doi.org/10.1002/(SICI)1521-3951(200001)217:1<357::AID-PSSB357>3.0.CO;2-J.

(10) Frauenheim, T.; Seifert, G.; Elsterner, M.; Hajnal, Z.; Jungnickel, G.; Porezag, D.; Suhai, S.; Scholz, R. A Self-Consistent Charge Density-Functional Based Tight-Binding Method for Predictive Materials Simulations in Physics, Chemistry and Biology. *physica status solidi (b)* **2000**, *217* (1), 41–62. https://doi.org/10.1002/(SICI)1521-3951(200001)217:1<41::AID-PSSB41>3.0.CO;2-V.

(11) Rego, L. G. C.; Batista, V. S. Quantum Dynamics Simulations of Interfacial Electron Transfer in Sensitized TiO $_2$ Semiconductors. *J. Am. Chem. Soc.* **2003**, *125* (26), 7989–7997. https://doi.org/10.1021/ja0346330.

(12) Monti, A.; Negre, C. F. A.; Batista, V. S.; Rego, L. G. C.; de Groot, H. J. M.; Buda, F. Crucial Role of Nuclear Dynamics for Electron Injection in a Dye–Semiconductor Complex. *J. Phys. Chem. Lett.* **2015**, *6* (12), 2393–2398.

(13) da Silva, R.; Hoff, D. A.; Rego, L. G. C. Coupled Quantum-Classical Method for Long Range Charge Transfer: Relevance of the Nuclear Motion to the Quantum Electron Dynamics. *J. Phys.: Condens. Matter* **2015**, *27* (13), 134206. https://doi.org/10.1088/0953-8984/27/13/134206.

(14) Menzel, J. P.; Papadopoulos, A.; Belić, J.; de Groot, H. J. M.; Visscher, L.; Buda, F. Photoinduced Electron Injection in a Fully Solvated Dye-Sensitized Photoanode: A Dynamical Semiempirical Study. *J. Phys. Chem. C* **2020**, *124* (51), 27965–27976. https://doi.org/10.1021/acs.jpcc.0c09551.

(15) Grimme, S.; Bannwarth, C.; Shushkov, P. A Robust and Accurate Tight-Binding Quantum Chemical Method for Structures, Vibrational Frequencies, and Noncovalent Interactions of

Large Molecular Systems Parametrized for All Spd-Block Elements (Z = 1–86). *J. Chem. Theory Comput.* **2017**, *13* (5), 1989–2009. https://doi.org/10.1021/acs.jctc.7b00118.

(16) Becke, A. D. A New Mixing of Hartree–Fock and Local Density-functional Theories. *J. Chem. Phys.* **1993**, *98* (2), 1372–1377. https://doi.org/10.1063/1.464304.

(17) Lee, C.; Yang, W.; Parr, R. G. Development of the Colle-Salvetti Correlation-Energy Formula into a Functional of the Electron Density. *Phys. Rev. B* **1988**, *37* (2), 785–789.

(18) Menzel, J. P.; Kloppenburg, M.; Belić, J.; Groot, H. J. M. de; Visscher, L.; Buda, F. Efficient Workflow for the Investigation of the Catalytic Cycle of Water Oxidation Catalysts: Combining GFN-XTB and Density Functional Theory. *Journal of Computational Chemistry* **2021**, *42* (26), 1885–1894. https://doi.org/10.1002/jcc.26721.

(19) Bakker, T. M. A.; Menzel, J. P.; Vreugdenhil, B.; Bouwens, T.; Mathew, S.; Buda, F.; Reek, J. N. H. Increased Photocurrent by Improving the Donating Properties of the Anchoring Group in P-Type Dye Sensitized Solar Cells. *to be submitted*.

(20) Nattestad, A.; Mozer, A. J.; Fischer, M. K. R.; Cheng, Y.-B.; Mishra, A.; Bäuerle, P.; Bach, U. Highly Efficient Photocathodes for Dye-Sensitized Tandem Solar Cells. *Nature Mater* **2010**, *9* (1), 31–35. https://doi.org/10.1038/nmat2588.

(21) Liu, Z.; Xiong, D.; Xu, X.; Arooj, Q.; Wang, H.; Yin, L.; Li, W.; Wu, H.; Zhao, Z.; Chen, W.; Wang, M.; Wang, F.; Cheng, Y.-B.; He, H. Modulated Charge Injection in P-Type Dye-Sensitized Solar Cells Using Fluorene-Based Light Absorbers. *ACS Appl. Mater. Interfaces* **2014**, *6* (5), 3448–3454. https://doi.org/10.1021/am405610b.

(22) Liu, Z.; Li, W.; Topa, S.; Xu, X.; Zeng, X.; Zhao, Z.; Wang, M.; Chen, W.; Wang, F.; Cheng, Y.-B.; He, H. Fine Tuning of Fluorene-Based Dye Structures for High-Efficiency p-Type Dye-Sensitized Solar Cells. *ACS Appl. Mater. Interfaces* **2014**, *6* (13), 10614–10622. https://doi.org/10.1021/am5022396.

# 7.A Appendix

### *7A.1 Computational Details*

Nuclear trajectories were prepared using GFN-xTB.[1] We have optimized Extended Hückel parameters, similar to chapter 6, on experimental oxidation potentials of the involved NDIs and the WOC in its $^1$[Ru(IV)-OH]$^+$ state. For the WOC, we use the Nernst equation to shift the oxidation potential vs NHE at pH=0 to a pH value of 7, translated towards absolute potential vs. an electron at rest in vacuum and used this as target HOMO energy of the respective oxidative state. For the LUMO energy, we used Δ SCF derived values given in table 7A.1. The Δ SCF calculations were performed using the B3LYP[2,3] XC-functional with D3 dispersion corrections and BJ-damping[4] and a TZP basis[5]. Relativistic effects were included using ZORA,[6–8] while implicit solvent water was modelled using COSMO.[9] The target values and results obtained with optimized Extended Hückel parameters can be found in table 7A.2.

***Table 7A.1:*** *Experimental Redox potentials vs. NHE and vacuum from CV measurements for the WOC (converted to ph=7 using Nernst equation) and ethylamine NDI dyes, approximated LUMO energy of the WOC with ΔSCF vs NHE and vacuum*

| **Molecule** | **$^1$[Ru(IV)-OH]$^+$** | **2NHEt-NDI** |
|---|---|---|
| **CV Oxidation Potential vs NHE (vs. vacuum)** | pH=1 : 1.25 V (5.69 V)[10]<br>pH=7 : 0.90 V (5.34 V) | 0.91 V (5.35 V)[11] |
| **CV Reduction Potential vs NHE (vs vacuum)** | - | -0.88 V (3.56 V)[11] |
| **ΔSCF Reduction Potential vs NHE (vs vacuum)** | -0.68 V (3.76 V) | - |

***Table 7A.2:*** *HOMO and LUMO energies for WOC and NDI: target values generated with a linear shift of -5.95 eV and values obtained with the optimized Hückel parameters.*

| **Molecule** | **Target values [eV]** | | **Optimized Hückel parameters [eV]** | |
|---|---|---|---|---|
| | HOMO | LUMO | HOMO | LUMO |
| WOC ($^1$[Ru(IV)-OH]$^+$) | -11.29 | -9.72 | -11.28 | -9.72 |
| 2NHEt-NDI | -11.30 | -9.51 | -11.31 | -9.52 |

## *7A.2 References*


(1) Grimme, S.; Bannwarth, C.; Shushkov, P. A Robust and Accurate Tight-Binding Quantum Chemical Method for Structures, Vibrational Frequencies, and Noncovalent Interactions of Large Molecular Systems Parametrized for All Spd-Block Elements (Z = 1–86). *J. Chem. Theory Comput.* **2017**, *13* (5), 1989–2009. https://doi.org/10.1021/acs.jctc.7b00118.

(2) Becke, A. D. A New Mixing of Hartree–Fock and Local Density-functional Theories. *J. Chem. Phys.* **1993**, *98* (2), 1372–1377. https://doi.org/10.1063/1.464304.

(3) Lee, C.; Yang, W.; Parr, R. G. Development of the Colle-Salvetti Correlation-Energy Formula into a Functional of the Electron Density. *Phys. Rev. B* **1988**, *37* (2), 785–789.

(4) Grimme, S.; Antony, J.; Ehrlich, S.; Krieg, H. A Consistent and Accurate Ab Initio Parametrization of Density Functional Dispersion Correction (DFT-D) for the 94 Elements H-Pu. *J. Chem. Phys.* **2010**, *132* (15), 154104. https://doi.org/10.1063/1.3382344.

(5) Van Lenthe, E.; Baerends, E. J. Optimized Slater-Type Basis Sets for the Elements 1–118. *J. Comput. Chem.* **2003**, *24*, 1142–1156.

(6) Lenthe, E. van; Baerends, E. J.; Snijders, J. G. Relativistic Regular Two-component Hamiltonians. *J. Chem. Phys.* **1993**, *99* (6), 4597–4610. https://doi.org/10.1063/1.466059.

(7) van Lenthe, E.; Baerends, E. J.; Snijders, J. G. Relativistic Total Energy Using Regular Approximations. *J. Chem. Phys.* **1994**, *101* (11), 9783–9792. https://doi.org/10.1063/1.467943.

(8) van Lenthe, E.; Ehlers, A.; Baerends, E.-J. Geometry Optimizations in the Zero Order Regular Approximation for Relativistic Effects. *J. Chem. Phys.* **1999**, *110* (18), 8943–8953. https://doi.org/10.1063/1.478813.

(9) Pye, C. C.; Ziegler, T. An Implementation of the Conductor-like Screening Model of Solvation within the Amsterdam Density Functional Package. *Theor. Chem. Acc.* **1999**, *101* (6), 396–408. https://doi.org/10.1007/s002140050457.

(10) Duan, L.; Bozoglian, F.; Mandal, S.; Stewart, B.; Privalov, T.; Llobet, A.; Sun, L. A Molecular Ruthenium Catalyst with Water-Oxidation Activity Comparable to That of Photosystem II. *Nature Chem.* **2012**, *4* (5), 418–423. https://doi.org/10.1038/nchem.1301.

(11) Sakai, N.; Mareda, J.; Vauthey, E.; Matile, S. Core-Substituted Naphthalenediimides. *Chem. Commun.* **2010**, *46* (24), 4225–4237. https://doi.org/10.1039/C0CC00078G.